Discovery of 72 new bright ZZ Ceti stars in the first three years of *TESS*

Alejandra D. Romero[1]⋆, S. O. Kepler[1], Larissa Antunes Amaral[1,2], Murat Uzundag[2], Zsófia Bognár[3,4], Madison VanWyngarden[5], Keaton J. Bell[6,7], J.J. Hermes[5], Andy Baran[8,9,10], Ingrid Pelisoli[11], Gabriela da Rosa Oliveira[1], Detlev Koester[12], Theylor Klippel[1], Luciano Fraga[13], Maja Vuckovic[2] and Stéphane Charpinet[14]
[1]*Instituto de Física, Universidade Federal do Rio Grande do Sul, 91501-970 Porto Alegre, RS, Brazil*
[2]*Instituto de Física y Astronomía, Universidad de Valparaíso, Gran Bretaña 1111, Playa Ancha, Valparaíso 2360102, Chile*
[3]*Konkoly Observatory, Eötvös Loránd Research Network (ELKH), Research Centre for Astronomy and Earth Sciences, Konkoly Thege Miklós út 15-17, H–1121, Budapest, Hungary*
[4] *MTA CSFK Lendület Near-Field Cosmology Research Group*
[5]*Department of Astronomy & Institute for Astrophysical Research, Boston University, 725 Commonwealth Ave., Boston, MA 02215, USA*
[6]*DIRAC Institute, Department of Astronomy, University of Washington, Seattle, WA-98195, USA*
[7]*NSF Astronomy and Astrophysics Postdoctoral Fellow*
[8]*ARDASTELLA Research Group, Institute of Physics, Pedagogical University of Cracow, ul. Podchorążych 2, 30-084 Kraków, Poland*
[9] *Embry-Riddle Aeronautical University, Department of Physical Science, Daytona Beach, FL 32114, USA*
[10] *Department of Physics, Astronomy, and Materials Science, Missouri State University, Springfield, MO 65897, USA*
[11]*Department of Physics, University of Warwick, Gibbet Hill Road, Coventry, CV4 7AL, UK*
[12]*Institut für Theoretische Physik und Astrophysik, Universität Kiel, D-24098 Kiel, Germany*
[13]*Laboratório Nacional de Astrofíisica LNA/MCTIC, 37504-364 Itajubá, MG, Brazil*
[14]*IRAP, Universite de Toulouse, CNRS, UPS, CNES, 14 avenue Edouard Belin, F-31400 Toulouse, France*

Accepted XXX. Received YYY; in original form ZZZ

ABSTRACT

We report the discovery of 72 new pulsating DA white dwarf stars, or ZZ Cetis, from the data obtained by the Transiting Exoplanet Survey Satellite (TESS) mission, from sectors 1 to 39, corresponding to the first 3 cycles. This includes objects from the Southern Hemisphere (sectors 1–13 and 27–39) and the Northern Hemisphere (sectors 14–26), observed with 120 s- and 20 s-cadence. Or sample includes 13 low-mass (M <0.45 $M_\odot$) and one extremely low-mass white dwarf, considering the photometric determinations of this parameter. In addition, we present follow-up observations from ground-based telescopes for 11 objects, which allowed us to detect a larger number of periods. For each object, we analysed the period spectra and performed an asteroseismological analysis, which allowed us to estimate the structure parameter of the sample, i.e., stellar mass, effective temperature and hydrogen envelope mass. The mean stellar mass for the sample of 57 objects with photometric mass above 0.45 $M_\odot$ is $\langle M_{\rm phot}\rangle = 0.614 \pm 0.037$ $M_\odot$, in agreement with the mean seismological mass of $\langle M_{\rm sis}\rangle = 0.628 \pm 0.015$ $M_\odot$ and with the mean stellar mass of a sample of 351 ZZ Cetis, being $\langle M_*\rangle = 0.644 \pm 0.034$ $M_\odot$. Our sample of 72 new ZZ Cetis increases the number of known ZZ Cetis in ~ 20 %.

Key words: stars: white dwarfs – stars: oscillations – surveys

1 INTRODUCTION

The Transiting Exoplanet Survey Satellite (*TESS*) was launched on 18 April 2018 (Ricker et al. 2014), with the primary mission of searching for exoplanets around bright target stars. TESS contains four cameras, with an entrance pupil of 10.5 cm, covering 24x24 deg, comprising 24x96 degrees, known as an observing sector. The wavelength coverage is from 600 to 1000 nm. Each camera is imaged on a 4096×4096 pixel CCD, resulting in 21” × 21” pixels.

Through nearly continuous stable photometry, as well as its extended sky coverage, TESS has made a significant contribution to the study of stellar pulsations in evolved compact objects (e.g. Bell et al. 2019; Wang et al. 2020; Bognár et al. 2020), including variable hydrogen-rich DA white dwarf stars. The activities related to compact pulsators, as white dwarf and subdwarf stars, are coordinated by the TESS Compact Pulsators Working Group (WG8).

Variable DA white dwarf or ZZ Ceti stars are the coolest pulsating white dwarfs, with an instability strip located between effective temperatures of $\sim$ 13 000 K and 10 000 K, depending on stellar mass (Hermes et al. 2017; Kepler & Romero 2017). Their photometric variations are due to surface temperature changes explained by spheroidal, non–radial g–modes pulsations with low harmonic degree ($\ell \leq 2$) and periods between 70 and 2000 s, with amplitude variations up to 0.3 mag. To date, there are $\sim$ 420 ZZ Cetis known

---

⋆ E-mail: alejandra.romero@ufrgs.br

(see for instance Córsico et al. 2019; Vincent et al. 2020; Guidry et al. 2021).

The driving mechanism for the excitation of the pulsations is a combination of the $\kappa-\gamma$ mechanism, acting on the hydrogen partial ionization zone at the base of the hydrogen envelope (Dolez & Vauclair 1981; Winget et al. 1982) for high effective temperatures, and the convective driving mechanism (Brickhill 1991; Goldreich & Wu 1999), which is dominant once a thick convective zone has developed in the outer layers. The ZZ Cetis can be classified into three groups, depending on the effective temperature and the stellar mass (Clemens 1993; Mukadam et al. 2006). The blue edge of the instability strip is defined by the hot ZZ Cetis, that exhibit a few modes with short periods (<350 s) and small amplitudes (1.5–20 mma). The pulse shape is sinusoidal or sawtooth shaped and is stable for decades. On the opposite side of the instability strip, the red edge, we find the cool DAV stars, showing several long periods (up to 1500 s), with large amplitudes (40–110 mma), and non-sinusoidal light curves that change dramatically from season to season due to mode interference. Mukadam et al. (2006) suggested introducing a third class, the intermediate ZZ Cetis, with mixed characteristics from hot and cool members.

In this work we present 72 new ZZ Ceti stars discovered from the first three cycles of TESS data, from sector 1 to sector 39, including 120 s- and 20 s-cadence data. In addition, we perform ground-based observations from three different telescopes for 11 objects, in most cases increasing the number of detected pulsation periods. This paper is organized as follows. We present the sample of 72 new ZZ Cetis, discovered from the TESS data in Section 2. We describe the sample selection and the data reduction for the TESS data and the ground-based observations in Section 3, including spectroscopic follow-up for 10 targets. In Section 4 we present the pulsation periods detected, and perform an asteroseismological study for our sample in Section 5. In Section 6 we present a study of the asteroseismological properties of the 72 ZZ Cetis presented in this work. We conclude in Section 7 by summarizing our findings.

2 NEW ZZ CETI STARS

We report the discovery of 72 new bright ZZ Ceti stars from the first three years of TESS data, sectors 1 to 39. The targets are listed in Table 1, along with the coordinates in J2000, G magnitude, effective temperature, surface gravity and stellar mass. The parameters are taken from various works, which used different techniques to determine the effective temperature and surface gravity or stellar mass. For those objects with more than one determination for their atmospheric parameters, we include those obtained using different techniques.

Subasavage et al. (2008) used low-resolution spectroscopy and multi-epoch VRI photometry combined with near-infrared JHK_S photometry from 2MASS. To determine the value of effective temperature, they used model atmospheres from Bergeron et al. (1995), assuming a $\log g = 8.0$, because trigonometric parallaxes were not available at the time.

The atmospheric parameters from Koester et al. (2009) were based on high-resolution spectra with UVES/VLT. The spectra were compared with theoretical model atmospheres from Koester (2009).

Gianninas et al. (2011) presented the results of an spectroscopic survey of bright ($V \leq 17.5$), hydrogen-rich white dwarf stars. To derived $T_{\rm eff}$ and $\log g$ they used an updated version of the pure hydrogen model atmospheres of Liebert et al. (2005), that consider energy transport by convection following the MLT/α = 0.8 prescription of the mixing length theory (Tremblay et al. 2010) and improved Stark broadening profiles of hydrogen lines from Tremblay & Bergeron (2009).

Limoges et al. (2013) used multi-band photometry to derived the distance (Giammichele et al. 2012), combined with follow-up spectroscopic observations for a sub-sample of identified white dwarf stars. They employed model atmospheres described in Bergeron et al. (1995), with the improvements discussed in Tremblay & Bergeron (2009). These are pure hydrogen, plane-parallel model atmospheres, that consider energy transport by convection following the ML2/α = 0.7 prescription of the mixing-length theory.

Raddi et al. (2017) performed follow-up spectroscopy for a sample of white dwarfs and hot subdwarfs, extracted from an all-sky catalogue of UV, optical and IR photometry and proper motion. For the determination of the effective temperature and surface gravity for the white dwarf stars, they employed model atmospheres from Koester (2010), which adopt a MLT/$\alpha =$ 0.8 mixing length prescription for convective atmospheres and the Stark broadening computed by Tremblay & Bergeron (2009).

Most of the data presented in Table 1 were taken from Gentile Fusillo et al. (2019), where they used the Gaia DR2 (Gaia Collaboration et al. 2018) magnitudes and parallax to determine the atmospheric parameters. They employed standard hydrogen atmosphere spectral models (Tremblay et al. 2011) including the L_α red wing absorption of Kowalski & Saumon (2006). To compute the stellar mass, they used the evolutionary sequences from Fontaine et al. (2001) with thick hydrogen layers and central composition C/O=50/50. The same procedure was employed by Fusillo et al. (2021) using data from Gaia DR3.

Finally, Kilic et al. (2020) and Vincent et al. (2020) rely on parallaxes from Gaia DR2 and photometry from the Sloan Digital Sky Survey (SDSS, Eisenstein et al. 2006; Kleinman et al. 2013; Kepler et al. 2019) and Panoramic Survey Telescope and Rapid Response System (Pan-STARRS, Chambers et al. 2016). They applied the photometric technique described in Bergeron et al. (1997), together with the pure hydrogen model atmospheres discussed in Bergeron et al. (2019) and reference therein. To derived $\log g$ and stellar mass they used white dwarf models similar to those described in Fontaine et al. (2001).

For the two objects TIC 0055650407 and TIC 0370239521 we determine the atmospheric parameter from the spectra we obtained with the SOAR telescope (see section 3.3 for details). We follow the fitting procedure described in detail in Kepler et al. (2019).

TIC 0345202693 is in a binary system with a possible M main sequence star which has a large contribution in the infrared wavelengths, with a value for $b_p - r_p = 0.637$ and an absolute magnitude of 11.83 from Gaia DR3. Based on spectroscopic observations from the SOAR telescope, we estimate the stellar mass and effective temperature of the white dwarf component.

The location of the 72 new ZZ Ceti stars in the $T_{\rm eff} - \log g$ plane is presented in Figure 1. For the targets with more than one determination for the atmospheric parameters in Table 1, we use that obtained from photometry and parallax from Gaia. The sample of ZZ Cetis stars known to date is depicted in this figure, and was extracted from the works of Bognar & Sodor (2016); Hermes et al. (2017); Su et al. (2017); Romero et al. (2019b); Vincent et al. (2020). The values for effective temperature and surface gravity derived from spectroscopy were corrected by 3D convection (Tremblay et al. 2013) for all objects. Most of the objects from our sample lay around the 0.6 $M_\odot$ track, showing canonical spectroscopic masses. Note that there are 13 objects with stellar masses in the range of $0.30 \leq M/M_\odot \leq 0.45$, which correspond to low-mass white dwarfs (Kilic et al. 2007; Istrate et al. 2016; Pelisoli & Vos 2019) and can harbour either a

Table 1. List of the 72 new ZZ Ceti found in TESS. Column 1 indicates the TIC identifier. The coordinates in J2000 are in columns 3 and 4, and the G magnitude is listed in column 5. The effective temperature, log *g* and stellar mass determinations are listed in columns 6, 7 and 8. Data taken from the works of (1) Gentile Fusillo et al. (2019), (2) Subasavage et al. (2008) (3) Raddi et al. (2017), (4) Koester et al. (2009), (5) Vincent et al. (2020), (6) Limoges et al. (2013), (7) Kilic et al. (2020), (8) (Gianninas et al. 2011), (9) (Kepler et al. 2019), (10) (Gentile Fusillo et al. 2021) and (11) This work

TIC	RA	DEC	G	$T_{\rm eff}$ [K]	log g	Mass [$M_\odot$]	Ref.
0005624184	093248.01	−374428.7	15.95	11243 ± 94	7.566 ± 0.018	0.411	1
0007675859	181222.74	+432107.6	16.27	11985 ± 250	8.462 ± 0.038	0.898	1
0008445665	162436.81	+321252.8	16.72	11200 ± 250	7.933 ± 0.038	0.565	1
0013566624	085134.85	−072828.3	16.44	13183 ± 290	8.156 ± 0.030	0.703	1
0020979953	153332.96	−020655.7	16.53	11859 ± 236	7.969 ± 0.039	0.587	1
· · ·	· · ·	· · ·	· · ·	11212 ± 54	7.89 ± 0.01	0.540	7
· · ·	· · ·	· · ·	· · ·	1132 ± 250	8.190 ± 0.022	0.713	9
0021187072	182606.04	+482911.3	16.28	11808 ± 228	7.235 ± 0.025	0.314	10
0024603397	052240.66	−080229.7	14.71	12024 ± 51	7.857 ± 0.009	0.526	1
0029862344	013715.16	−172722.7	15.25	11613 ± 192	8.14 ± 0.06	0.682	2
0033717565	040536.39	−762828.1	16.52	10767 ± 250	7.633 ± 0.038	0.431	1
0046847635	092916.70	−084032.2	16.75	12217 ± 358	8.034 ± 0.062	0.626	1
0055650407	045527.27	−625844.6	14.99	11917 ± 250	7.956 ± 0.038	0.580	1
· · ·	· · ·	· · ·	· · ·	12134 ± 67	7.906 ± 0.002	0.556	11
0063281499	222858.15	−310553.7	15.61	11678 ± 84	8.00 ± 0.02	0.604	1
· · ·	· · ·	· · ·	· · ·	12200 ± 200	8.02 ± 0.06	0.616	3
0065144290	071114.04	−251815.0	14.47	11208 ± 180	8.12 ± 0.060	0.670	1
0072637474	· · ·	· · ·	15.92	11769 ± 250	7.54 ± 0.038	0.413	4
0079353860	211815.52	−531322.7	15.92	11123 ± 250	7.944 ± 0.038	0.571	1
0116373308	030211.43	+480013.6	16.33	11733 ± 250	8.004 ± 0.035	0.607	1
· · ·	· · ·	· · ·	· · ·	11551 ± 60	· · ·	0.614	5
0141976247	062527.47	−754041.7	15.58	13286 ± 250	8.213 ± 0.038	0.739	1
0149863849	174349.28	−390825.9	13.53	11604 ± 206	8.087 ± 0.027	0.657	10
0156064657	003723.75	−482155.9	16.60	10098 ± 102	7.274 ± 0.033	0.314	1
0158068117	060052.91	−463041.1	16.09	12833 ± 123	7.420 ± 0.020	0.373	1
0188087204	104627.80	−251215.8	16.83	10228 ± 143	7.607 ± 0.047	0.421	1
0207206751	031318.66	−560735.0	14.62	10968 ± 250	7.996 ± 0.038	0.601	1
0220555122	025621.34	−632840.2	15.87	11980 ± 250	8.179 ± 0.038	0.715	1
0229581336	180115.3	+721849.0	16.05	14120 ± 240	7.387 ± 0.026	0.369	1
0230029140	192853.8	+610548.7	16.45	11372 ± 176	7.967 ± 0.031	0.585	1
0230384389	190319.56	+603552.6	15.04	11366 ± 89	8.09 ± 0.014	0.658	1
0231277791	024918.23	−533435.4	16.46	11596 ± 250	8.058 ± 0.038	0.639	1
0232979174	143417.88	+653959.5	16.14	12811 ± 234	7.765 ± 0.026	0.481	1
0238815671	215211.62	−633236.4	16.12	11693 ± 250	7.944 ± 0.038	0.573	1
0261400271	065101.30	−803409.6	14.90	13670 ± 250	8.399 ± 0.038	0.859	1
0273206673	043350.99	+485039.2	15.35	11367 ± 236	7.965 ± 0.039	0.584	1
0282783760	131426.82	+173209.2	16.30	11960 ± 250	8.013 ± 0.038	0.613	1
0304024058	092256.24	−681648.8	16.10	11521 ± 173	7.956 ± 0.029	0.579	1
0313109945	140540.57	+743859.3	15.59	9059 ± 134	7.49 ± 0.04	0.380	1
0317153172	232232.11	−831314.2	16.47	11813 ± 314	8.032 ± 0.042	0.624	10
0317620456	192182.42	+274025.4	15.04	10566 ± 67	· · ·	0.603	7
· · ·	· · ·	· · ·	· · ·	11060 ± 163	8.10 ± 0.05	0.66	6
0343296348	174344.00	−742437.5	15.85	11597 ± 150	7.968 ± 0.023	0.586	10
0344130696	183708.31	−765905.9	15.39	10829 ± 116	7.177 ± 0.018	0.293	10
0345202693	184828.03	−742760.0	16.56	11332 ± 250	· · ·		10*
0353729306	024029.66	+663637.1	15.60	11874 ± 250	8.019 ± 0.038	0.617	1
0370239521	218400.53	−535837.2	14.65	11191 ± 978	8.23 ± 0.44	0.733	11
0380298520	201343.26	+341356.0	15.68	11511 ± 250	8.387 ± 0.038	0.848	1
· · ·	· · ·	· · ·	· · ·	11440 ± 118	· · ·	0.854	5
0394015496	215823.88	−585353.8	15.81	11688 ± 250	8.012 ± 0.038	0.612	1
0415337224	035454.26	+074606.3	16.54	16380 ± 308	7.87 ± 0.06	0.55	8
· · ·	· · ·	· · ·	· · ·	10600 ± 300	· · ·	0.563	10
0428670887	115840.65	−202951.2	16.01	11718 ± 250	8.057 ± 0.038	0.639	1
0610337553	005546.72	−150452.7	17.36	10400 ± 300	· · ·	0.498	10
0631161222	012624.73	−711712.0	16.96	11435 ± 362	7.934 ± 0.059	0.566	10
0631344957	021328.27	−643708.9	16.98	11574 ± 311	7.995 ± 0.050	0.602	10
0632543879	022823.39	+134727.3	16.98	11300 ± 300	· · ·	0.580	10
0651462582	030733.09	−465316.3	17.08	10800 ± 300	· · ·	0.531	10
0661119673	044258.31	+323715.63	17.37	11640 ± 453	7.949 ± 0.083	0.575	1

Table 1 – *continued*

TIC	RA	DEC	G	$T_{\rm eff}$ [K]	log g	Mass [$M_\odot$]	Ref.
0683837451	045827.11	−654003.4	17.40	6953 ± 73	7.560 ± 0.034	0.391	10
0685410570	050011.50	−504612.4	17.04	11266 ± 325	7.974 ± 0.058	0.580	1
0686044219	042148.96	−355849.8	17.13	11298 ± 33	7.989 ± 0.06	0.597	1
0712406809	063917.24	+011329.5	16.22	10952 ± 89	8.033 ± 0.013	0.623	7
0724128806	053724.22	−804549.7	17.48	9881 ± 214	7.587 ± 0.065	0.412	1
0733030384	053203.91	−653609.9	16.89	12586 ± 168	8.009 ± 0.022	0.612	?
0800153845	085507.25	+063540.0	16.656	10400 ± 300	...	0.549	10
0804835539	085457.51	−764621.9	16.906	15296 ± 476	8.078 ± 0.046	0.659	10
0804899734	083258.10	−760105.9	17.40	12033 ± 399	8.022 ± 0.058	0.619	1
0951016050	121411.95	−345845.9	17.03	11292 ± 263	7.974 ± 0.051	0.589	10
1001545355	141353.96	+713612.6	16.99	11244 ± 232	7.653 ± 0.036	0.439	10
1102242692	152809.16	+553916.1	17.09	11180 ± 184	7.86 ± 0.07	0.530	8
1102346472	145323.52	+595056.2	17.16	11217 ± 250	7.97 ± 0.038	0.589	9
1173423962	144114.41	−384629.7	17.38	10719 ± 414	7.920 ± 0.093	0.556	10
1108505075	154455.68	−690910.4	16.993	11369 ± 225	7.918 ± 0.043	0.557	10
1201194272	163358.75	+591206.6	17.13	11238 ± 290	7.962 ± 0.057	0.582	1
1309155088	165426.50	+235241.5	16.99	10700 ± 91	8.033 ± 0.013	0.622	7
1989258883	201439.52	−565501.7	16.62	11138 ± 176	7.970 ± 0.038	0.586	1
1989866634	204311.73	−461048.5	17.38	11135 ± 315	7.945 ± 0.075	0.572	1
2026445610	212421.14	−631012.4	17.27	11308 ± 211	7.960 ± 0.048	0.581	1
2055504010	224554.79	−450058.9	16.84	11092 ± 184	7.898 ± 0.046	0.546	1
...	...	...	...	11550 ± 178	8.07 ± 0.05	0.650	6

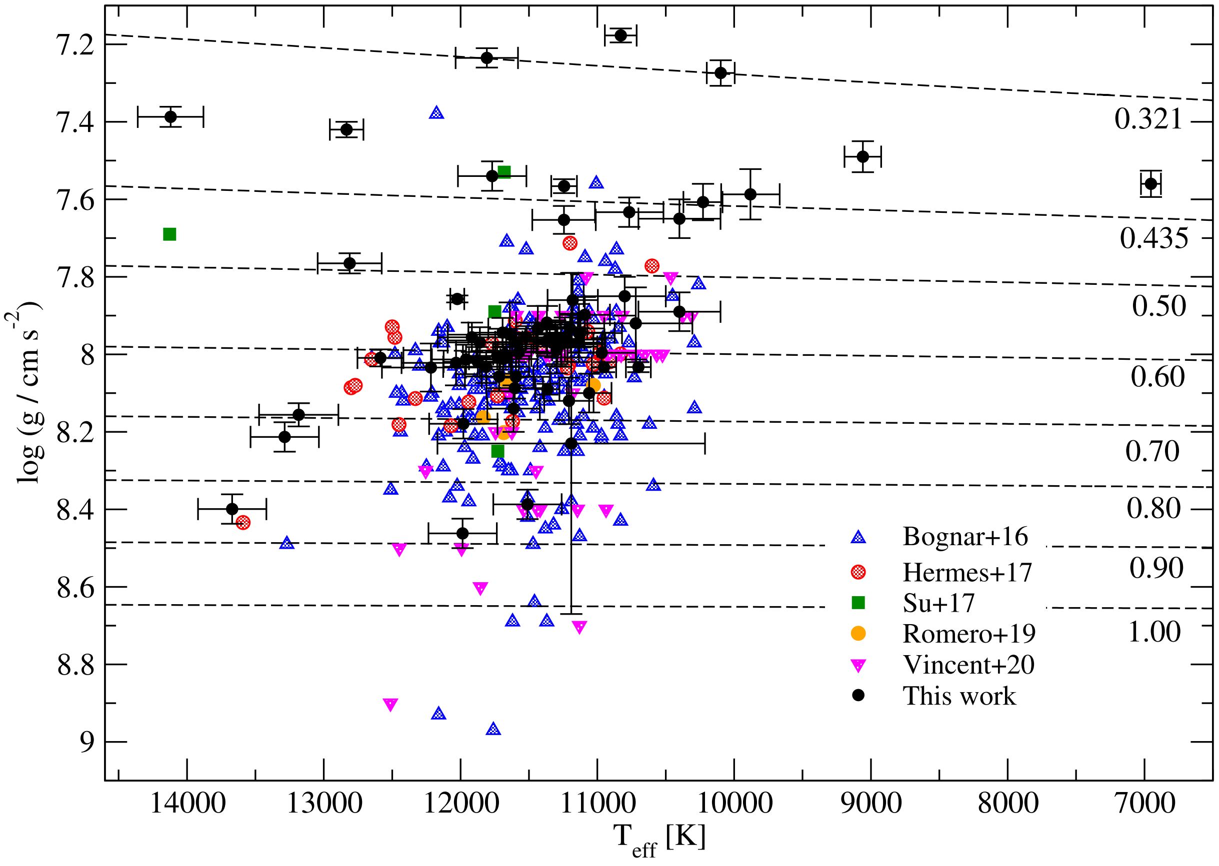

Figure 1. Distribution of ZZ Ceti stars on the $T_{\rm eff}$ − log g plane. The coloured symbols correspond to known ZZ Ceti stars, taken from Bognar & Sodor (2016) (blue up-triangle), Hermes et al. (2017) (red circle), Su et al. (2017) (green square), Romero et al. (2019b) (orange circle) and Vincent et al. (2020) (magenta down-triangle). The objects observed in this work are depicted with black circles. We include evolutionary tracks (dashed lines) with stellar masses between 0.435 $M_\odot$ and 0.9 $M_\odot$ from Romero et al. (2019a) and 0.321 $M_\odot$ Istrate et al. (2014).

He/C/O- or a He-core, depending on the evolution of the progenitor star. TIC 0345202693 has a photometric stellar mass below 0.3 $M_\odot$, being a possible Extremely low-mass white dwarf variable. Finally, the are three objects with spectroscopic masses above 0.8 $M_\odot$, being TIC 0007675859 the more massive object of our sample, with a photometric mass of 0.898 $M_\odot$.

3 OBSERVATIONS AND DATA REDUCTION

We selected the targets for the sample of DA white dwarf stars from Gentile Fusillo et al. (2019) with G ≤ 17.5 that were targeted by the TESS satellite in sectors 1 to 39, with 120 s and/or 20 s-cadence. This includes both the southern (sector 1-13 and 27-39) and the northern (sector 14-26) hemispheres, with 120 s cadence. From sector 27, the satellite turned back to the southern hemisphere, and data with 20 s cadence was available for a subset of objects. In addition, we performed photometric observations from ground based telescopes with a cadence smaller than 45 s for a small subset (11) to confirm variability and to look for new periodicities. Finally, we performed spectroscopic observations for another subset to confirm that the objects were indeed DA white dwarf stars. These data were used to improve the determination of the atmospheric parameters for the targets. A detail description of the observations and data analysis is presented in the sections below.

3.1 TESS data

We downloaded the light curves from The Mikulski Archive for Space Telescopes, which is hosted by the Space Telescope Science Institute (STScI)[1] in FITS format. The data contained in the FITS files were processed based on the Pre-Search Data Conditioning pipeline (Jenkins et al. 2016). We extracted times and fluxes (PDCSAP FLUX) from the FITS files. The times are given in barycentric corrected dynamical Julian days (BJD – 2457000, corrected for leap seconds, see Eastman et al. 2010). The fluxes were converted into fractional variations from the mean, that is, differential intensity $\Delta I/I$, and transformed into amplitudes in parts-per-thousand (ppt). The ppt unit corresponds to the milli-modulation amplitude (mma) unit[2] used in the past. We sigma-clipped the data at 5σ to remove the outliers that appear above five times the median of intensities, that is, that depart from the (local) mean by 5σ.

We calculated their Fourier transforms (FTs) and examined them for pulsations or binary signatures above the 1/1000 false-alarm probability, calculated reshuffling the data 1000 times, but maintaining the same time base, and calculating their Fourier transform, selecting the highest peak. For pre-whitening, we employed our customized tool, in which, using a nonlinear least-squares (NLLS) method, we simultaneously fit each pulsation frequency in a waveform $A_i \sin(\omega_1 t + \phi)$, with $\omega = 2\pi/P$, and P the period. This iterative process was run starting with the highest peak until no peak appeared above the 0.1% false-alarm probability (FAP) significance threshold. We analyzed the concatenated light curve from different sectors, if observed. The FAP was again calculated by randomizing the observations, that is, shuffling the observations one thousand times and recalculating the FTs. We calculated the amplitude at which there was a 0.1%= 1/1000 probability of any peak being due to noise (e.g. Kepler 1993).

The third year of the TESS mission started with sector 27. From this sector on, besides the 120 s-cadence data, some objects were observed with 20 s-cadence, increasing the frequency resolution. Figure 2 shows the spectral window for the 120 s and 20 s cadence data from TESS for one sector of TIC 030402405 data.

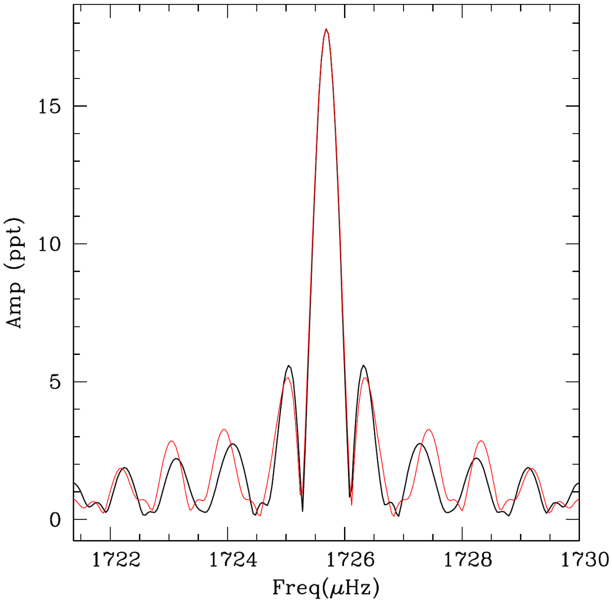

Figure 2. Spectral window for the 120 s (black) and 20 s cadence (red) data from single sector TESS data for TIC 0304024058.

3.2 Ground-based observations

Ground-based follow-up observations for 11 objects were performed with three different telescopes, the 1 m at Konkoly Observatory in Hungary, the 1.6 m Pekin-Elmer telescope at the Pico do Dias Observatory in Brazil, and the 4.1 m SOAR telescope in Chile. The journal of observations is presented in Table 2.

3.2.1 Konkoly Observatory

We performed the observations with the 1 m Ritchey–Chrétien–Coudé telescope located at the Piszkéstető mountain station of Konkoly Observatory, Hungary. We obtained data with a Spectral Instruments 1100S CCD camera in white light. The exposure times were selected to be either 30 or 45 s. We reduced the raw data frames the standard way utilizing IRAF tasks: we performed bias and flat field corrections before the aperture photometry of field stars. We fitted low-order polynomials to the resulting light curves, correcting for long-period instrumental and atmospheric trends, and finally, we converted the observational times of every data point to barycentric Julian dates in barycentric dynamical time ($\mathrm{BJD_{TDB}}$) using the applet of Eastman et al. (2010)[3].

3.2.2 SOAR telescope

We employed Goodman image mode on the 4.1-m Southern Astrophysical Research (SOAR) Telescope in Chile. We used read out mode 200 Hz ATTN2 with the CCD binned 2×2, with a ROI reduced

---

[1] http://archive.stsci.edu/

[2] 1 mma= 1/1.086 mmag= 0.1 % = 1 ppt; see, e.g., Bognar & Sodor (2016).

[3] http://astroutils.astronomy.ohio-state.edu/time/utc2bjd.html

Table 2. Journal of observations from ground-based facilities. We list the target, telescope, date of observation, exposure time and total observation time, in columns 1, 2, 3, 4 and 5, respectively. The sizes of the telescopes are 1-m, 4.1-m and 1.6-m, for the 1-m Konkoly observatory, 4.1-m SOAR and 1.6-m OPD, respectively.

TIC	Telescope	Run stars (UT)	t_{exp} (s)	Δt (h)
0007675859	Konkoly	2020-08-20	30	5.45
		2020-08-21	30	5.95
		2020-08-22	30	4.28
		2020-08-23	45	3.96
		2020-08-25	45	5.89
		2020-08-26	45	6.14
0020979953	OPD	2020-06-14	17	3.4
		2020-11-27	10	3.36
0055650407	SOAR	2020-11-26	10	3.72
0232979174	Konkoly	2021-07-05	45	5.05
		2021-07-06	45	5.38
		2021-07-07	30	4.81
0273206673	Konkoly	2020-09-11	30	4.68
		2020-10-08	30	6.88
		2020-12-11	45	4.63
		2020-12-13	30	4.23
		2020-12-14	30	3.50
		2020-12-14	45	2.53
0282783760	OPD	2021-06-14	17	3.1
0304024058	SOAR	2020-12-02	10	3.46
0313109945	Konkoly	2020-06-11	30	2.32
		2020-06-13	30	4.71
		2020-07-04	30	4.49
		2020-07-05	30	5.18
		2020-07-07	30	4.87
0370239521	OPD	2020-06-14	17	3.4
		2020-11-27	10	3.36
1989866634	OPD	2021-05-09	40	3.1
		2021-06-12	40	3.38
2055504010	OPD	2021-06-13	20	2.6
		2021-06-14	20	3.2

to 800×800. All observations were obtained with a red blocking filter S8612. The integration times varied from 10 to 15 s, depending on the magnitude of the object and the weather conditions. Note that with this configuration, the read-out time is ∼ 5 s.

We reduced the data with the software IRAF, and perform aperture photometry with DAOFOT. We extracted light curves of all bright stars that were observed simultaneously in the field. Then, we divided the light curve of the target star by the light curves of all comparison stars to minimize effects of sky and transparency fluctuations. To look for periodicities in the light curves, we calculate the Fourier transform (FT) using the software `PERIOD 04` (Lenz & Breger 2004). We accepted a frequency peak as significant if its amplitude exceeds the 0.1% FAP. We then use the process of pre-whitening the light curve by subtracting out of the data a sinusoid with the same frequency, amplitude, and phase of the highest peak and then computing the FT for the residuals. We redo this process until we have no new significant signals.

3.2.3 Pico dos Dias Observatory

We used the IxON camera on the 1.6-m Perkin Elmer Telescope at the Pico dos Dias Observatory, in Brazil. We used a red blocking filter BG40. The integration times varies from 20 to 45 s, depending on the magnitude of the object, with a read-out time of less than 1 s.

Table 3. Log of spectroscopic observations.

TIC	Date-Time (UT-Start)	Exp. (sec)	S/N (at 4200 Å)	Telescope/Inst.
0238815671	2021-06-19 08:56:46	500	100	SOAR/GOODMAN
0370239521	2021-06-19 08:44:43	350	115	SOAR/GOODMAN
0394015496	2021-06-19 09:30:38	500	130	SOAR/GOODMAN
0428670887	2021-06-18 02:54:04	1200	120	SOAR/GOODMAN
055650407	2020-12-07 00:34:50	720	50	SOAR/GOODMAN
063281499	2019-08-22 01:05:01	600	65	DUPONT/B&C
065144290	2021-03-05 04:45:01	400	100	SOAR/GOODMAN
1989258883	2021-06-19 07:02:00	900	105	SOAR/GOODMAN
207206751	2021-03-05 01:29:51	900	150	SOAR/GOODMAN
220555122	2021-03-05 01:00:52	1200	100	SOAR/GOODMAN
261400271	2021-03-05 04:01:19	500	100	SOAR/GOODMAN

The data reduction process is similar to that described in the previous section.

3.3 Spectroscopy with Dupont and SOAR

We perform spectroscopic observations for eleven objects from our sample of 72 new ZZ Ceti stars, to confirm they were DA white dwarfs and to improve the determinations of the atmospheric parameters.

TIC 063281499 was observed with the Boller and Chivens (B&C) spectrograph mounted at the 2.5-meter (100-inch) Iréne du Pont telescope at Las Campanas Observatory in Chile[4]. The B&C spectra were obtained using the 600 lines/mm grating corresponding to the central wavelength of 5000 Å, and covering a wavelength range from 3427 to 6573 Å. We used a 1 arcsec slit, which provided a resolution of 3.1 Å. The data from Dupont@B&C was reduced and analysed using *PyRAF*[5] (Science Software Branch at STScI 2012) procedures with the following way: First, bias correction and flat-field correction have been applied. Then, the pixel-to-pixel sensitivity variations were removed by dividing each pixel with the response function. After this reduction was completed, we have applied wavelength calibrations using the frames obtained with the internal HeAr comparison lamp. In a last step, flux calibrations were applied using the standard star EG 274. The signal-to-noise ratio (SNR) of the final spectra is around 65 (see Table 3).

The majority of our southern spectroscopic observations have been obtained using the Southern Astrophysical Research (SOAR) Telescope and the Goodman spectrograph (Clemens et al. 2004), situated at Cerro Pachón, Chile. We use the 400 l/mm grating with the blaze wavelength 5500 Å(M1: 3000-7050 Å) with a slit of 1 arcsec. This setup provides a resolution of about 5.6 Å. The data reduction has been partially done by using the pipeline[6] including overscan, trim, slit trim, bias and flat corrections. For cosmic rays identification and removal, we used an algorithm as described by Pych (2004), which is embedded in the pipeline. The extraction and calibration of the spectra were carried out similarly as for Dupont@B&C using standard *PyRAF* tasks.

---

[4] For a description of instrumentation, see: `http://www.lco.cl/?epkb_post_type_1=boller-and-chivens-specs`

[5] `http://www.stsci.edu/institute/software_hardware/pyraf`

[6] `https://github.com/soar-telescope/goodman_pipeline`

4 PERIODS AND DATA ANALYSIS

In this section we present the results from the light curve analysis of the 72 new bright ZZ Ceti stars. The values of the detected periods are listed in Table 4 for the results based on TESS data. We also include the corresponding sectors and the amplitude detection limit for false-alarm probability FAP=1/1000. Figure 3 show the Fourier Transform (top panel) and the complete light-curve (bottom panel) for the object TIC 313109945. This object shows seven peaks above the FAP=1//1000 confidence level, depicted as a red line. A long period of 6.60 d is also present at low frequencies.

The results from ground based observations are presented in Table 5. From the 11 objects observed from ground-based telescopes, 8 of them show periodic variability above the FAP=1/1000 limit on the ground data. For TIC 0055650407 we confirm some of the periods detected from TESS data, but no additional periods were detected, as can be seen from Figure 5. This is also the case for TIC 2055504010. For TIC 0304024058 the same periods as in the TESS data were detected from ground-base observations, as shown in Figure 4. For TIC 0273206673, TIC 0282783760 and TIC 1989866634 we detected additional periodicities from ground-based observations, and also confirmed the periods identified by using TESS data. In particular, for TIC 0370239521, the period spectrum present in the FT from the Pico dos Dias observatory are not the same periods detected by TESS data, however, the period values are in the same range around $\sim$ 800 s. Only one period is present on both data sets, with a period of $\sim$ 279 s.

4.1 Super-Nyquist

TESS acquires data with an even time sampling between observations, Δt. Even time sampling causes each significant signal to produce an infinite set of alias signals in the periodogram, each reflected across multiples of the Nyquist frequency of $f_{\rm Nyq} = 1/(2\Delta t)$. Without external constraints on intrinsic signal frequencies, any of these frequency aliases can describe the data equally well. Deviations from strictly even time series caused by the barycentric timestamp corrections are minor (Murphy 2015), and strong aliasing is observed in the TESS data.

With pulsation periods observed to be as short as 70 s, ZZ Cetis can pulsate with intrinsic signals above up to three times the 120 s cadence Nyquist frequency of 4166.67 μHz, resulting in up to four viable aliases for each pulsation mode. Including the incorrect alias frequency in an asteroseismic analysis will corrupt the inference. Without additional data, frequency aliases are usually favored that appear most consistent with the ensemble of studied ZZ Ceti pulsation spectra. In some cases, coherence of a pulsation signal can be used as an argument for certain aliases, and modes with periods longer than roughly 800 s tend to vary in phase and amplitude on ~day timescales (Montgomery et al. 2020).

From sector 27 on, the TESS satellite observed some objects with 20 s cadence, effecting a Nyquist frequency sufficiently above ZZ Ceti pulsation frequencies to avoid Nyquist ambiguities. For targets without such data, ground-based follow-up photometry with a different cadence can be used to select the correct alias (e.g., Bell et al. 2017).

As an example, in Figure 4 we show the FT for TIC 0304024058 for 120 s cadence TESS data (top panel), ground-based observation from SOAR telescope with ~15 s-cadence (middle panel) and 20 s cadence TESS data (bootm panel). The red horizontal line indicates the detection limit and the inset in each plot depicts the spectral window. For the 120 s cadence data in the top panel, the blue vertical line corresponds to the Nyquist frequency. Note that in this case, there are four significant peaks in the super-Nyquist region, being the peak with a period of 151.34 s the one with the highest amplitude. However, these peaks are not seen in the ground-based observations, where only the peaks corresponding to periods between 400 s and 620 s are present. The same result is obtained when we include the 20 s cadence data from TESS. Thus, in this case, the sub-Nyquist aliases are confirmed to correspond to the intrinsic pulsation frequencies by ground-based observations and short cadence data.

A different result is found for TIC 0055650407 as shown in Figure 5. The FT corresponding to the 120 s cadence TESS data shows two peaks with super-Nyquist frequencies, in particular one corresponding to a period of 200.08 s (see top panel). The same period is also present in the FT for the SOAR telescope data, shown in the middle panel of Figure 5, which confirms the existence of this period. On the other hand, the peak corresponding to the period of 320.76 s is not detected in the SOAR data, probably due to the much shorter SOAR observation run (3.72 h). Finally, the period with 200.08 s is also confirmed by the 20 s cadence TESS data, shown in the bottom panel of Figure 5. In addition, there is another peak at high frequencies with a corresponding period of 126.84 s that was not apparent in the 120-s data since the period is close to the exposure time.

4.2 TIC 0020979953

TIC 0020979953 was part of the target list for the TESS mission, but no 120 s or 20 s cadence data was taken for this object to date. We observed TIC 0020979953 from the Pico do Dias observatory in two nights in 2020 (see Table 2) for a total of 6.76 h. The light curve and FT are presented in Figure 6 for the night of 2020-06-14 that spans for 3.4 h. From this dataset we detected three short periods of 259.68 s, 285.30 s and 365.64 s, compatible with a blue edge ZZ Ceti (Mukadam et al. 2006).

5 ASTEROSEISMOLOGICAL ANALYSIS

In this section we present an asteroseismological analysis of all objects presented in Tables 4 and 5.

The DA white dwarf models used in this work are the result of full evolutionary computations of the progenitor stars, from the zero-age main sequence, through the hydrogen and helium central burning stages, thermally pulsating and mass-loss asymptotic giant branch phase and finally the planetary nebulae domain. They were generated using the LPCODE evolutionary code (see Althaus et al. 2010; Renedo et al. 2010; Romero et al. 2015, for details). The stellar mass values go from 0.493 $M_\odot$ to 1.05 $M_\odot$, with a hydrogen layer mass in the range of $\sim 4 \times 10^{-4}$ to $\sim 10^{-10}$ M_*, depending on the stellar mass. Non-radial adiabatic g-mode pulsations were computed using the adiabatic version of the LP-PUL pulsation code described in Córsico & Althaus (2006). We employ an extended version of the model grid presented in Romero et al. (2019b) that includes new cooling sequences with stellar masses between 0.5 and 1.0 $M_\odot$, along with approximately eight hydrogen layer values for each sequence, depending on the stellar mass (Klippel et al. 2021, in preparation). For each object we search for an asteroseismological representative model that best matches the observed periods. To this end, we seek

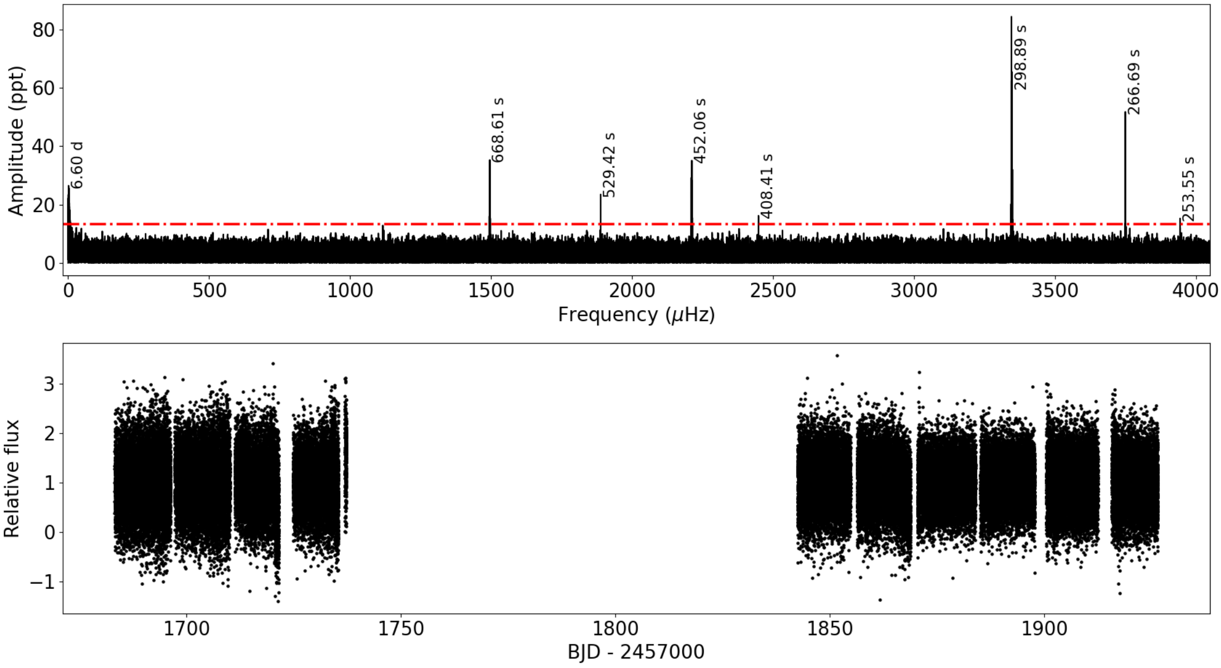

Figure 3. Fourier Transform for TIC 0313109945, for data with 120 s cadence corresponding to sectors 14, 15, 20 and 21. The horizontal red line corresponds to the false-alarm probability FAP=1/1000 detection limit for the combined data.

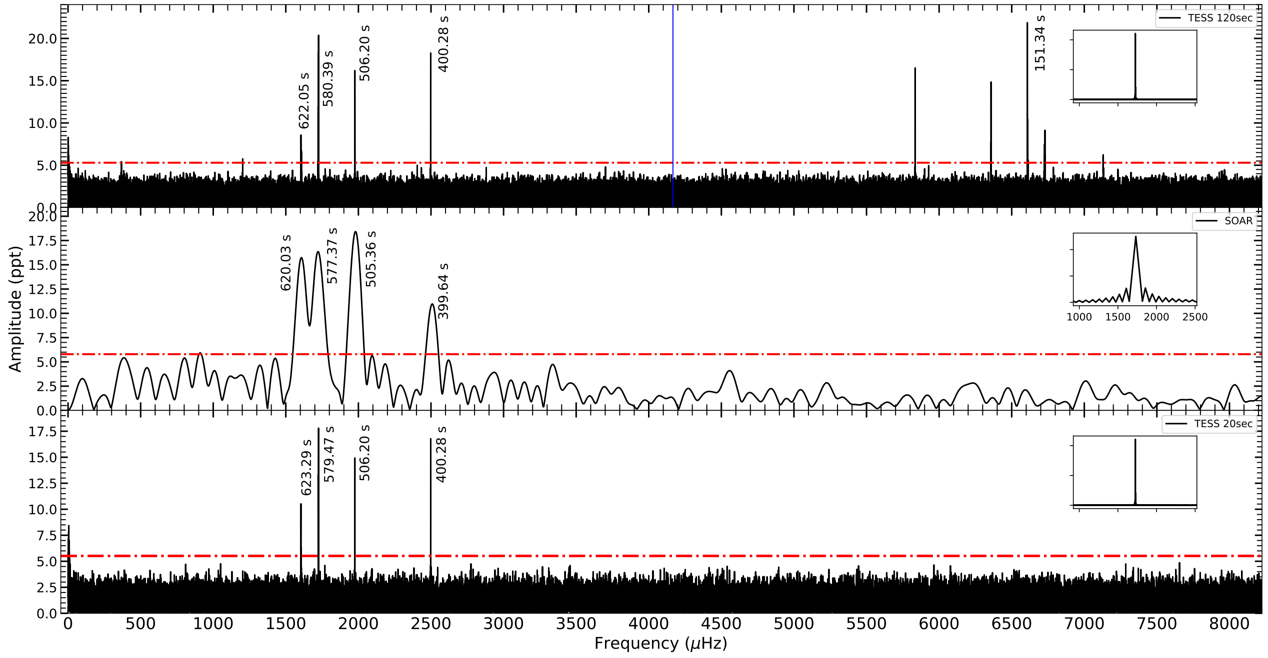

Figure 4. Fourier Transform for TIC 0304024058 for three different data sets. The result base on 120 s - cadence TESS data is depicted in the top panel, while the bottom panel shows the FT for the 20 s -cadence TESS data. The FT based on the SOAR telescope data (10 s integration time) is shown in the middle panel. The amplitude at FAP=1/1000 detection limit in each case is indicated by the horizontal dashed line and the spectral window for each case is depicted as an inset plot. The blue vertical line in the top panel indicate the value of the Nyquist frequency.

Table 4. Detected periods for the new ZZ Cetis. For each object we list the sectors where the target was observed by the TESS satellite, indicating the 20 s cadence runs with "f" (col 2), the value of the amplitude detection limit for false-alarm probability FAP(1/1000) (col 3), and the list of periods compatible with stellar pulsations in white dwarfs (col 4). In column 5 we include comments on the observations.

TIC	sector	FAP(1/1000)	Π [s] (A [ppt])
0005624184	f35-f36	4.583	503.99s (6.279), 445.92 (4.769), 431.31 (4.663)
0007675859	25,26	9.381	353.25 (27.39), 356,09 (14.32), 360.32 (9.33), 798.66 (12.08), 743.44 (11.09)
0008445665	24,25	8.777	812.763 (18.199), 638.223 (15.047), 1018.484 (8.974), 578.053 (8.922), 356.874 (8.839)
0013566624	34	7.013	421.87 (8.917), 407.63 (7.827)
0021187072	25,26	3.633	1076.8617 (6.785), 1074.2723 (4.994), 1070.7403 (3.924)
0024603397	5,32	1.942	262.65 (3.129)
0029862344	03,f30	2.674	737.566 (3.369), 857.43 (4.03), 898.93 (2.74), 352.09 (2.22)
0033717565	27-29,32,35-36,39	3.585	364.92 (10.334), 526.98 (4.471)
0046847635	35		415.81 (9.656)
0055650407	11-13,f27-f39	0.478	320.76 (1.65), 262.46 (7.21), 200.08 (4.42), 126.84 (1.84)
0063281499	01,f28	2.942	320.515 (8.542), 383.70 (2.93)
0065144290	7,33-34	4.870	278.171 (7.272)
0072637474	03,f30	2.509	901.16 (2.687), 814.44 (2.559), 966.24 (2.546)
0079353860	1,27	3.464	945.19 (4.29), 842.43 (3.50), 525.56 (3.60)
0116373308	18	40.823	361.8 (59.3)
0141976247	1-8,10-13,27-34,f35-f37	0.706	115.94623h (1.29616), 261.72 (0.860)
0149863849	f39	1.785	397.98 (6.8995), 397.04 (6.429), 491.21 (7.449), 568.09 (3.136), 487.36 (3.074)
0156064657	29	6.036	1418.05 (13.45), 1546.556 (6.05)
0158068117	5-7,32-33	1.976	268.45 (2.480)
0188087204	36	6.827	742.55 (14.437), 657.53 (13.312), 661.35 (9.661), 541.35(7.290), 500.84 (6.872)
0207206751	29-30	0.926	893 (2.1), 775 (2.0), 860 (1.5), 627 (1.5), 905 (1.4), 1271 (1.2), 864 (1.1), 810 (1.1)
0220555122	1-3,28,30	2.231	243.894 (2.52), 539.450 (2.36), 137.54 (2.29)
0229581336	14-25	2.203	1106.46 (3.329), 519.02 (2.288), 420.18 (2.200)
0230029140	14-26	3.160	288.89 (8.63), 311.06 (9.01), 784.77 (7.19), 400.35 (4.64), 364.41 (4.36)
0230384389	14-26	0.752	457.17 (2.46), 707.92 (2.57), 493.86 (1.67), 749.61 (1.35), 1633.57 (1.05), 1284.58 (0.66)
0231277791	29-f30	2.798	721.44 (12.7), 711.56 (8.6), 497.74 (5.9), 762.28 (3.8)
0232979174	14-16,21-23	2.336	282.66 (3.542)
0238815671	01,f27-28	4.371	257.586 (9.22), 287.288 (6.86)
0273206673	19	13.154	583.4 (33.65), 827.2 (32.74), 698.9 (19.33)
0261400271	1,4,7,8,11-13,f27-f28,f31,f34	0.701	3052.55 (1.455), 295.70 (0.745), 382.92 (0.728)
0282783760	23	6.431	257.76 (8.923)
0304024058	10-11		623.428 (2.119), 579.483 (4.392), 506.193 (2.615), 400.278 (2.469)
0313109945	14,15,20-22	13.389	298.9 (82), 266.7s,452.1s,668.6s,529.4s,408.4s,253.6s
0317153172	27,f39	5.089	786.78 (7.836), 791.96 (6.395), 512.05 (6.531)
0317620456	26	6.068	15601.32 (10.003), 261.10 (7.436), 429.23 (6.163), 2429.96 (6.229)
0343296348	12,13	9.919	288.273 (16.663), 287.765 (10.013), 287.259 (10.485)
0344130696	12-13,f39	1.995	1018.68 (2.432), 1057.48 (2.172)
0353727306	18-19,25	9.826	545.8 (65.41), 470.2 (26.39), 404.84 (17.93)
0370239521	1	0.520	820.43 (1.86), 809.26 (1.18), 575.76 (0.83), 563.65 (0.61), 297.24 (0.53)
0380298520	14,15	9.129	550.40 (14.681)
0394015496	01,27-f28	2.264	310.27 (4.64), 309.79 (5.38), 309.31 (4.08)
0415337224	5	7.563	936.55 (15.508), 550.81 (10.968), 953.712 (8.777)
0428670887	10	9.189	200.85 (17.92) or 298.14 (17.40)
0610337553	30	14.194	759.60 (32.359), 922.68 (15.416)
0631161222	27,29	7.550	679.82 (27.330), 708.00 (13.408), 403.63 (11.983), 466.62 (10.399), 367.44 (10.177)
0631344957	28,29	6.909	363.14 (9.012)
0632543879	31	12.995	461.33 (18.608), 784.54 (16.252), 735.89 (16.079), 652.31 (14.095), 736.24 (13.039)
0651462582	31	11.548	818.15 (17.552), 683.85 (13.728), 1018.36 (11.881)
0661119673	19	42.848	626.41 (82.359)
0683837451	27-35,37-39	5.687	1036.28 (6.1053)
0685410570	31-32	7.365	965.50 (10.229), 812.91 (9.049), 556.66 (7.408)
0686044219	31-32	7.871	913.00 (18.749), 875.82 (8.951), 736.04 (17.364)
0712406809	f33	7.887	828.222 (14.607), 510.291 (11.157), 872.998 (9.609), 115.924 (8.650), 624.284 (7.923)
0724128806	27-38,31,34	9.149	290.18 (10.341)
0733030384	27-29,31-36	5.914	275.49 (7.353), 411.28 (6.265)
0800153845	34	16.656	878.34 (42.926), 712.44 (17.893)
0804835539	37	13.658	1007.21 (15.733)
0804899734	30,33,37-39	11.177	394.71 (24.025), *558.78 (11.308)*
0951016050	37	10.393	818.45 (15.063), 644.63 (10.626)
1001545355	14,20-22	10.597	516.18 (17.787), 761.14 (15.776), 955.19 (15.467), 1058.10 (11.082), 249.97 (10.989)
1102242692	16,22,24	7.152	1009.04 (9.555), 406.17 (7.366)

Table 4 – *continued*

TIC	sector	FAP(1/1000)	Π [s] (A [ppt])
1102346472	15-16,22-23	11.077	458.13 (27.733)
1173423962	38	28.321	618.36 (38.359), 794.80 (30.334)
1108505075	39	34.744	693.55 (45.470), 1323.54 (36.691), 1801.77 (36.088)
1201194272	14-16,18?26	6.899	840.92 (8.373)
1309155088	25	12.935	769.06 (17.292)
1989258883	27	7.292	909.04 (10.783)
1989866634	27	14.279	613.97 (22.222)
2026445610	27	14.690	825.25 (25.556), 815.53 (20.521), 317.74 (15.166)
2055504010	28	12.813	990.32 (14.562), 818.73 (12.921), 774.69 (13.246)

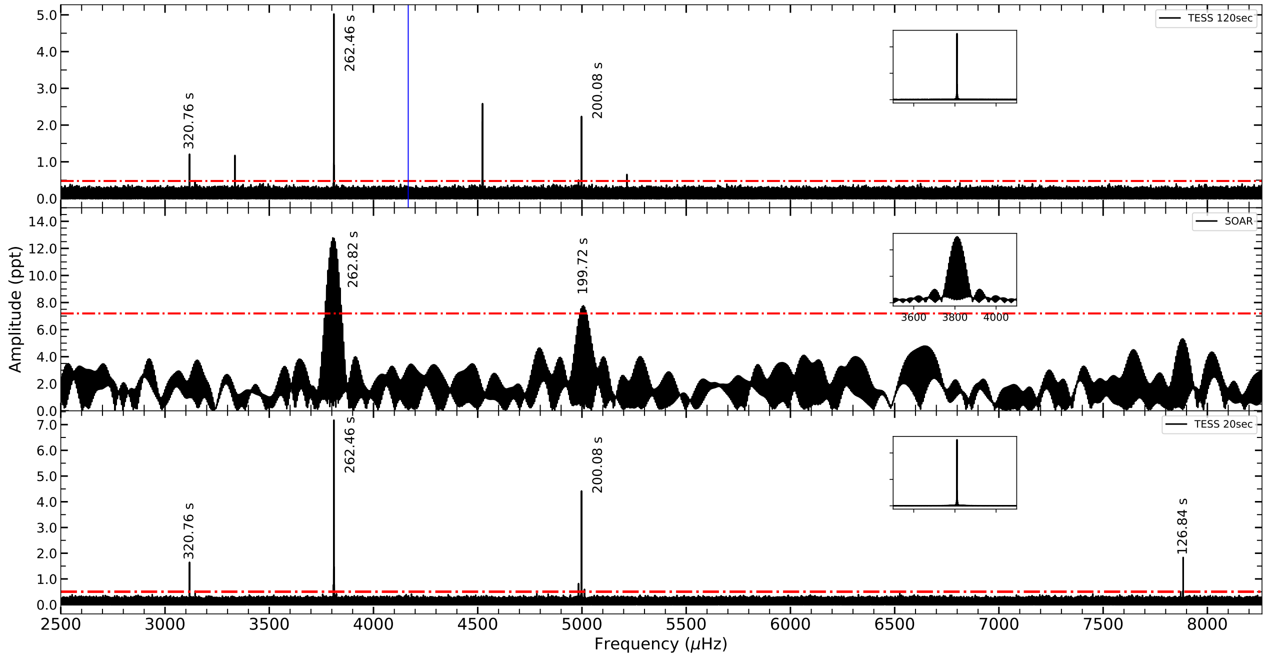

Figure 5. Fourier Transforms for TIC 0055650407 (same as Fig. 4)

for the theoretical model that minimizes the quality function given by Castanheira & Kepler (2008),

$$S(M_*, M_{\rm H}, T_{\rm eff}) = \sqrt{\sum_{i=1}^{N} \min\left[\frac{[\Pi_i^{\rm th} - \Pi_i^{\rm obs}]^2 A_i}{\sum_{i=1}^{N} A_i}\right]}, \qquad (1)$$

where N is the number of observed periods, $\Pi_i^{\rm th}$ is the theoretical period that better fits the observed period $\Pi_i^{\rm obs}$, and the amplitudes A_i are used as weights for each period. In this way, the period fit is more influenced by those modes with larger observed amplitudes. For the 8 objects with both TESS and ground-based data, we combine the list of periods to perform the asteroseismological fit. We do not consider periods corresponding to harmonics or linear combinations, nor those modes that show super-Nyquist frequencies that were not confirmed by short-cadence observations. For the stars with spectroscopic mass below the minimum value of our C/O-core grid (0.493 $M_\odot$) we also perform an initial asteroseismological fit with He-core white dwarf models with stellar masses from 0.17 to 0.45 $M_\odot$ (Córsico et al. 2012), considering only canonical hydrogen envelopes and $\ell = 1$ modes.

The results of our asteroseimological fits are presented in Table 6. For each object we list the stellar mass, thickness of the hydrogen envelope and effective temperature for the seismological model, in columns 2, 3, and 4, respectively. Column 5 shows the values for the theoretical periods along with the corresponding harmonic degree ℓ, and radial order k. Finally, the value of the quality function S is listed in column 9. The first model listed is the one we choose to be the best-fitting model for that particular object.

5.1 Rotation Period

White dwarf stars are considered slow rotators, with rotation periods between a few hours and several days (see for instance Kepler & Romero 2017). For five objects of our sample, we detected rotational splittings in the FT, corresponding to possible triplets. Thus, by considering the frequency separation we can estimate the rotation

Table 5. Detected periods from ground based observations. The TIC number, period, amplitude are listed in columns 1, 2 and 3, respectively. The identification for each mode is listed in the last column.

TIC	Π [s]	A (ppt)	ID
0020979953	259.68	7.36	f_1
	285.30	6.25	f_2
	365.64	4.07	f_3
0055650407	262.82	12.78	f_1
	199.72	7.78	f_2
0273206673	1029.0	49	f_1
0282783760	257.587	2.2	f_1
	283.417	1.3	f_2
	308.958	1.5	f_3
0304024058	620.03	13.53	f_1
	577.37	16.75	f_2
	505.36	18.42	f_3
	399.64	10.60	f_4
0370239521	894.895	18.68	f_1
	733.530	10.65	f_2
	447.205	7.05	$2f_1$
	776.761	6.93	f_3
	934.291	6.51	f_4
	297.611	6.32	$3f_1$
1989866634	613.960	55.86	f_1
	305.918	15.10	$2f_1$
	570.388	14.70	f_2
	362.833	14.21	f_3
	896.050	12.02	f_4
	228.647	10.54	f_5
	501.381	7.96	f_6
	294.374	7.38	$f_1 + f_2$
	975.113	7.26	f_7
2055504010	772.94		f_1

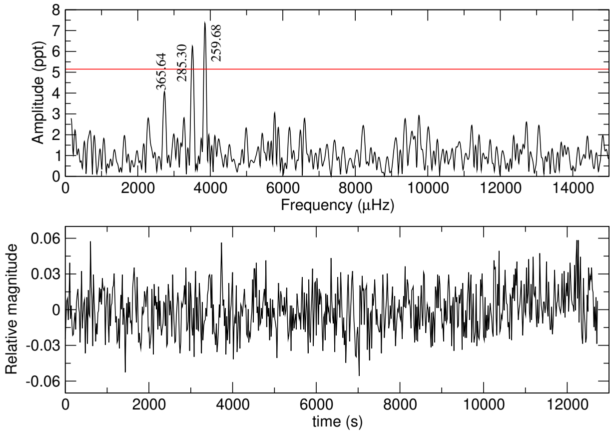

Figure 6. FT and light curve, top and bottom panel respectively, for TIC 0020976653 based on data obtained from the Pico dos Dias observatory on 2020-06-14. The data spans for 3.4 h, with an integration time of 17 s.

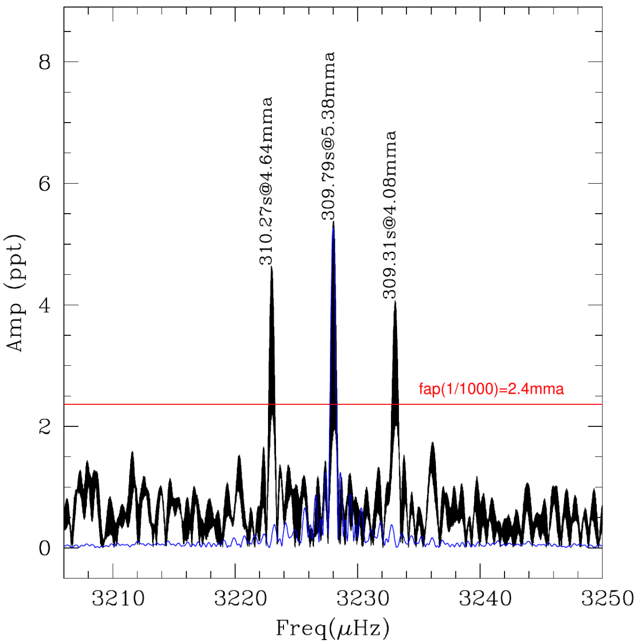

Figure 7. FT for TIC 0394015496 showing the three peaks corresponding to the triplet centred at 309.79 s for the combined data set. In blue the corresponding spectral window of a single peak.

period of the white dwarf star, following the equation (Cowling & Newing 1949; Ledoux 1951):

$$\frac{1}{P_{\rm rot}} = \frac{\Delta\nu_{k,\ell,m}}{m(1 - C_{k\ell})} \tag{2}$$

where m is the azimuthal number and $C_{k\ell}$ is the rotational splitting coefficient given by:

$$C_{k,\ell} = \frac{\int_0^{R_*} \rho r^2 [2\xi_r \xi_t + \xi_t^2 dr}{\int_0^{R_*} \rho r^2 [\xi_r^2 + \ell(\ell+1)\xi_t^2] dr} \tag{3}$$

where ρ is the density, r is the radius and ξ_r and ξ_t are the radial and horizontal displacement of the material.

The list of objects with detected $\ell = 1$ multiplets is presented in Table 8. We list the periods corresponding to the multiplet, the $C_{k\ell}$ and the mean rotation period. In Figure 7 we show an example of a triplet detected with TESS data for TIC 0394015496.

For TIC 0007675859 and TIC 0021187072, additional to the periods listed in table 4, the FT from the TESS data showed peaks at low frequencies, corresponding to periods of 12.315 h and 22.62 h, respectively. However, these long periodicities do not seem compatible with the values obtained for the mean rotation period for these objects.

6 ANALYSIS OF THE SAMPLE

In this section we analyse the main results of our sample of 72 new bright ZZ Ceti stars. In Figure 8 we compare the values for the effective temperature from photometry + parallax (x-axis) and asteroseismology (y-axis). We consider that the internal uncertainties from the asteroseismological fitting procedure are 100 K, 200 K, and 300 K, for effective temperatures, below 11 400 K, between 11 400

Table 6. Best fit model for the new ZZ Cetis using the list of observed modes. The stellar mass, hydrogen envelope and effective temperature are listed in columns 2, 3 and 4, respectively. We list the theoretical periods in column 5, along with the harmonic degree and the radial order. The value of the quality function S in seconds is listed in column 6.

TIC	$M/M_\odot$	$-\log(M_H/M_*)$	$T_{\rm eff}$ [K]	Π[s] (ℓ, k)	S [s]
0005624184	0.493	4.85	11190	503.71 (1,7), 446.70 (2,12), 431.35 (1,16)	0.46
0007675859	0.660	8.82	11710	356.26 (1,4), 798.51 (1,12), 742.93 (1,13)	0.28
· · ·	0.800	5.67	11660	356.33 (1,6), 799.19 (1,18), 743.00 (2,30)	0.37
0008445665	0.675	4.35	10970	811.70 (1,17), 639.25 (1,13), 358.27 (2,12), 575.46 (2,21), 1019.48 (2,39)	1.51
0013566624	0.705	6.15	12770	421.87 (1,4)	0.001
0021187072	0.660	5.55	11680	1074.2711 (1,21)	0.001
0024603397	0.542	6.83	12500	262.65 (1,2)	0.004
0029862344	0.609	8.33	11370	737.29 (1,12), 857.39 (1,14), 89890 (2,27)	0.12
0033717565	0.609	5.74	12530	262.72 (1,3), 198.70 (1,2), 322.30 (2,9)	0.99
0046847635	0.686	4.87	11930	415.82 (1,7)	0.002
0063281499	0.542	4.25	11610	320.37 (1,4), 384.76 (1,6)	0.60
0065144290	0.632	4.46	11480	278.17 (1,4)	0.0006
0072637474	0.542	4.94	11720	812.13 (1,14), 901.66 (1,16), 966.44 (1,17)	1.36
0079353860	0.686	5.25	11390	945.54 (1,18), 842.57 (1,16), 525.10 (1,9)	0.35
0116373308	0.609	8.33	11590	361.81 (1,4)	0.01
· · ·	0.609	5.54	12160	361.78 (1,5)	0.02
0141976247	0.686	8.82	12910	261.71 (1,3)	0.01
0149863849	0.660	4.41	11380	397.99 (2,13), 419.15 (2,14), 569.41 (2,20), 487.83 (2,17)	0.55
0156064657	0.493	6.84	10860	1418.07 (1,22), 1546.64 (1,24)	0.05
· · ·	0.358	3.26	9640	1418.71 (1,20), 1547.54 (1,22)	1.04
0158068117	0.493	8.82	12150	268.453 (1,2)	0.003
· · ·	0.303	2.90	9350	268.436 (1,2)	0.001
0188087204	0.493	4.16	10640	743.05 (1,12), 657.69 (1,8), 544.00 (1,8), 500.07 (2,14)	1.19
0207206751	0.570	4.28	10950	894.12 (2,30), 775.00 (2,26), 859.69 (1,16), 626.64 (1,11), 905.59 (1,17) 1115.36 (2,38), 1277.72 (1,25), 864.29 (2,29), 809.88 (1,15)	2.55
0220555122	0.686	6.34	11690	243.908 (1,3), 539.408 (1,9)	0.03
0229581336	0.493	4.45	11310	1106.45 (2,34), 519.59 (2,15), 420.19 (1,6)	0.31
· · ·	0.400	3.18	10460	1106.60 (1,17), 514.61 (1,7), 421.31 (1,5)	1.75
0230029140	0.593	5.04	11190	287.01 (1,3), 313.76 (1,4), 784.77 (1,14), 400.97 (1,6), 360.26 (2,10)	2.26
0230384389	0.525	9.25	11410	(457.61 (1,5), (708.73 (1,10), 495.23 (2,12), 751.67 (2,20), 1283.10 (1,20), 1632.01 (2,46)	1.24
0231277791	0.570	5.45	11300	721.23 (1,13), 713.02 (2,23), 498.55 (1,8), 762.44 (2,25)	086
0232979174	0.660	5.35	12020	282.66 (1,4)	0.004
· · ·	0.493	3.72	11710	282.67 (1,3)	0.01
0238815671	0.690	5.26	11630	257.792 (1,3), 286.891 (1,4)	0.30
0261400271	0.820	5.78	12390	295.25 (1,5), 382.68 (1,7)	0.36
0313109945	0.675	9.25	9890	300.19 (1,3), 266.11 (1,2), 450.54 (2,11), 685.84 (2,19), 583.53 (2,16), 410.63 (2,10), 250.03 (2,5)	1.74
0317153172	0.621	6.34	11900	786.67 (2,25), 791.88 (1,14), 512.27 (1,8)	0.15
0317620456	0.632	4.46	11010	260.86 (1,3), 429.24 (1,7)	0.19
0343296348	0.548	4.27	11310	287.766 (1,3)	0.001
0344130696	0.632	9.34	11180	1018.70 (1,17), 1057.84 (1,18)	0.31
0345202693	0.705	4.88	10670	587.86 (1,11), 789.31 (1,16), 833.79 (1,17), 833.79 (1,17)	0.51
0353729306	0.690	6.94	11680	545.96 (1,9), 470.63 (1,7), 404.13 (2,12)	0.38
0380298520	0.745	9.24	11550	549.86 (1,9)	0.10
0394015496	0.593	6.11	11570	309.79 (1,3)	0.002
0415337224	0.609	4.85	10100	936.88 (2, 32), 550.73 (1,9), 953.11 (1,18)	0.37
0428670887	0.609	5.24	11500	298.14 (1,4)	0.004
0610337553	0.609	6.33	10970	759.49 (1,13), 922.81 (1,16)	0.12
0631161222	0.609	5.44	11400	368.60 (1,5), 403.39 (1,6), 467.10 (1,7), .79,27 (1,12), 708.31 (1,13)	0.60
0631344957	0.550	4.84	11550	363.144 (1,5)	0.004
0632543979	0.660	5.15	11250	461.54 (2,15), 783.90 (1,15), 736.26 (2,25), 652.00 (2,22), 797,03 (1,14)	0.50
0651462582	0.593	5.79	10780	817.49 (1,14), 683.29 (1,11), 1019.36 (1,18)	0.74
0661119673	0.570	4.55	11600	626.42 (1,11)	0.01
0683837451	0.570	5.34	10790	1036.28 (1,18)	0.004
0685410570	0.609	4.95	10900	965.62 (1,18), 812.60 (1,15), 557.09 (1,9)	0.30
0686044219	0.639	4.12	11130	913.75 (1,19), 735.99 (1,15), 875.08 (1,18)	0.58

Table 6 – *continued*

TIC	M/M$_\odot$	M$_H$/M$_*$)	T$_{\rm eff}$ [K]	Π[s] (ℓ, k)	S [s]
0712406809	0.646	4.12	10820	827.83 (1,17), 510.53 (2,18), 872.93 (1,18), 118.57 (1,1), 623.51 (1,12)	1.15
0724128806	0.542	6.36	10910	290.18 (1,3)	0.003
· · ·	0.251	2.92	10410	290.19 (1,2)	0.01
0733030384	0.660	6.24	12390	275.48 (1,4), 411.63 (1,6)	0.24
0800153845	0.593	7.34	11780	877.99 (1,14), 712.38 (1,11)	0.29
0804835539	0.609	4.45	10990	1007.210 (1,20)	0.00
0804899734	0.609	5.35	11780	394.82 (1,6)	0.002
0951016050	0.660	4.86	10850	818.58 (1,12), 644.56 (1,16)	0.11
1001545355	0.542	6.13	11380	516.47 (1,14), 763.42 (1,22), 955.84 (1,28), 1055.98 (1,31)	1.52
1102242692	0.609	5.44	11200	1009.13 (1,19), 406.18 (1,6)	0.07
1102346472	0.548	4.27	10970	458.13 (1,7)	0.002
1108505075	0.579	5.34	11310	693.40 (1,12), 1323.63 (1,25), 1801.95 (1,35)	0.14
1173423962	0.690	7.14	10940	618.45 (1,10), 794.75 (1,14)	0.08
1201194272	0.609	4.11	11470	840.92 (1,17)	0.003
1309155088	0.609	4.19	10710	769.05 (1,15)	0.01
1989258883	0.609	6.04	11110	909.03 (1,16)	0.01
2026445610	0.525	3.79	11240	825.42 (1,15), 317.77 (1,4)	0.09

Table 7. Best fit model for the new ZZ Cetis using the list of modes from TESS and ground based observations. The stellar mass, hydrogen envelope and effective temperature are listed in columns 2, 3 and 4, respectively. We list the theoretical periods in column 5, along with the harmonic degree and the radial order. The value of the quality function S in seconds is listed in column 6. *No variability detected with TESS down to FAP=1/1000.

TIC	M/M$_\odot$	$-\log(M_H/M_*)$	T$_{\rm eff}$ [K]	Π[s] (ℓ, k)	S [s]
0020979953	0.632	8.33	11130	259.768 (1,2), 285.268 (1,3), 365.572 (1,4)	0.07
	0.593	3.93	12200	258.592 (1,3), 285.587 (1,4), 365.787 (1,6)	0.73
0055650407	0.570	3.82	12600	316.93 (1,5), 262.34 (1,3), 203.39 (2,5), 125.17 (1,1)	2.28
	0.542	5.63	12980	320.95 (1,4), 263.45 (1,3), 201.75 (2,4), 125.17 (2,2)	1.25
0273206673	0.560	3.77	11340	581.7 (1,10), 826.9 (1,16), 697.3 (1,13), 1030.5 (2,37)	1.42
0282783760	0.593	3.93	12270	258.138 (1,3), 284.804 (1,4), 307.688 (1,4)	1.06
	0.493	4.35	11710	257.835 (2,6), 283.944 (1,3), 308.375 (2,8)	0.45
0304024058	0.542	4.15	12020	623.336 (2,20), 579.093 (1,10), 504.593 (2,16), 400.219 (2,12)	0.80*
	0.593	6.33	11400	623.527 (2,19), 578.500 (1,9), 506.816 92,15), 401.334 (2,11)	0.83*
0370239521	0.770	8.66	11010	822.34 (1,15), 806.91 (2,27), 576.79 (1,10), 565.95 (2,18), 274.34 (2,7), 895.47 (1,17), 732.69 (2,24), 779.20 (2,26), 932.76 (1,18)	2.05
	0.721	5.08	11240	821.03 (2,31), 808.78 (1,17), 578.19 (2,21), 569.39 (1,11), 276.93 (1,4), 896.39 (1,19), 729.89 (1,15), 772.40 (2,29), 932.48 (1,20)	2.57
1989866634	0.820	7.36	10960	613.81 (1,12), 568.43 (1,11), 364.26 (2,12), 899.66 (2,33), 227.90 (1,3), 500.76 (1,9), 973.80 (2,36)	1.47
	0.609	4.75	11250	614.31 (1,11), 572.38 (2,19), 359.98 (2,11), 895.59 (2,31), 227.89 (2,6), 495.11 (1,8), 975.76 (1,19)	2.03
2055504010	0.705	5.75	11030	990.45 (1,20), 818.45 (1,16), 774.90 (2,27)	0.21

Table 8. List of objects with detected rotational splittings. For each object we list the periods that form the multiplet (col 2), the value of the $C_{k\ell}$ obtained from the asteroseismologial representative model (col 3) and the mean rotation period (col 4).

TIC	Π [s]	$C_{k\ell}$	$\bar{P}_{\rm rot}$
0007675859	353.25, 356.09, 360.32	0.487359	5.20 h
0021187072	1070.74, 1074.27, 1076.86	0.494833	2.24 d
0231277791	711.86, 721.44	0.454462	7.88 h
0343296348	287.259, 287.765, 288.273	0.45776	1.02 d
0394015496	309.31, 309.79, 310.27	0.463199	1.24 d

and 11 800 K, and higher than 11 800 K, respectively. The uncertainties for the photometric effective temperature are taken from Table 1. As can be seen from this figure, the data is clustering around the 1:1 correspondence line. The out-layers correspond to those objects with photometric mass below 0.45 M$_\odot$ and those with photometric effective temperature higher than 14 000 K. The Pearson coefficient is r = 0.5004, which indicates a moderate correlation. We do not expect a full correlation since both determinations come from different data sets, being the three photometric filters and parallax for the photometric determination, and the detected period spectrum for the seismological determination. In particular, the Gaia photometric filters are red filters, thus the determination of effective temperature for hot objects as white dwarf stars will have large uncertainties.

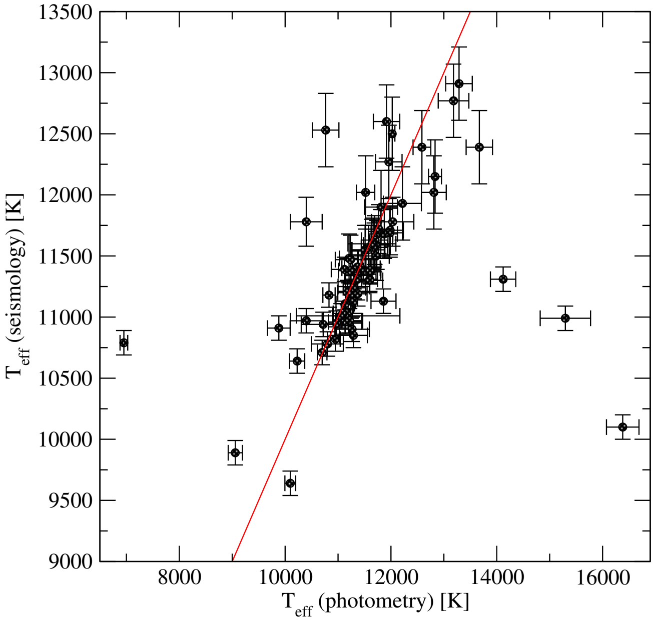

Figure 8. Comparison between the effective temperature obtained from Gaia photometry + parallax (see Table 1) and the asteroseismological fit (see Table 6). The red line indicates the 1:1 correspondence.

Figure 9 shows the comparison between the stellar mass from photometry + parallax (x-axis) and the value obtained from our seismological fit. Note that we do not include TIC 0345202693 since this object has no reliable photometric parameters due to its main sequence companion. The uncertainties for the seismological mass correspond to internal uncertainties from the fitting procedure. Although the points are around the 1:1 correspondence line, there is a large scatter around the 1:1 correspondence line. The Pearson coefficient is r=0.5244, corresponding to a moderate correlation.

The larger discrepancies between the photometric and seismological masses appear for the objects with photometric mass below 0.45 $M_\odot$, highlighted in blue in Figure 9. Since our model grid do not consider white dwarf models with stellar masses below 0.493 $M_\odot$, we do not expect an agreement between the two determinations.

The mass distribution for 71 objects is show in Figure 10, where we show the histograms for the photometric (top panel) and the seismological (low panel) stellar mass. As expected, the mass distribution from photometry extends further to lower stellar masses, than the one from asteroseismology. In both cases, most of the object show stellar masses between 0.5 ans 0.7 $M_\odot$.

The mean photometric mass is $\langle M_{\rm phot}\rangle$ = 0.572± 0.035 $M_\odot$, while for the seismological mass, the value is $\langle M_{\rm seis}\rangle = 0.613\pm0.015$ $M_\odot$. Even though both values agree within the uncertainties, the seismological mean mass is ~ 7% higher than the photometric value. If we consider only the 57 objects with photometric masses larger than 0.49 $M_\odot$, the values are $\langle M_{\rm phot}\rangle$ = 0.614± 0.037 $M_\odot$, and $\langle M_{\rm seis}\rangle$ = 0.628±0.015 $M_\odot$, with an agreement within 1σ. Finally, these values for the photometric and seismological mean mass are in agreement with the mean mass of 351 known ZZ Ceti stars shown in Figure 1 with coloured symbols, being $\langle M_*\rangle = 0.644\pm0.034$ $M_\odot$.

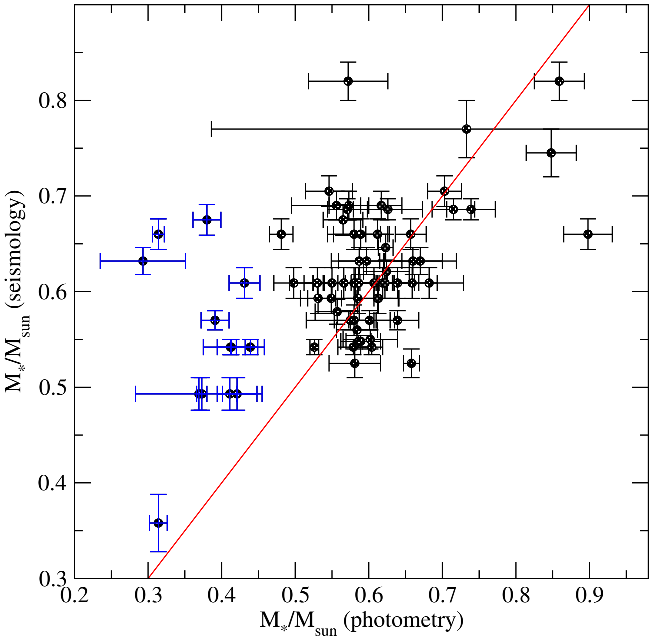

Figure 9. Comparison between the stellar mass obtained from Gaia photometry + parallax (see Table 1) and the asteroseismological fit (see Table 6). The red line indicates the 1:1 correspondence. The objects with photometric masses below 0.45 $M_\odot$ are highlighted in blue.

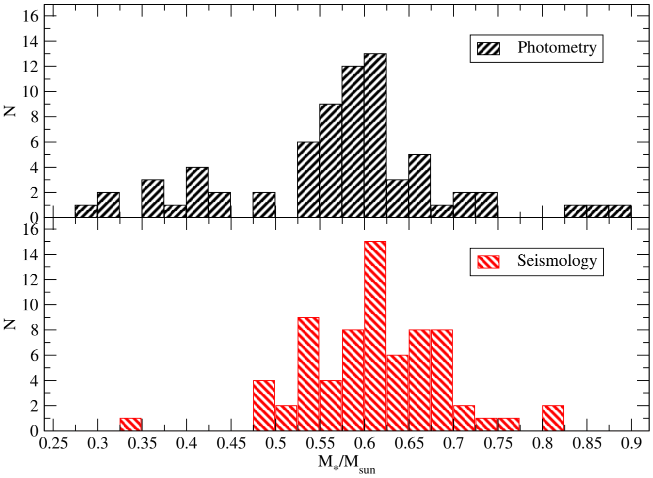

Figure 10. Histograms showing the distribution of the photometric (top) and seismological (bottom) stellar mass.

7 CONCLUSIONS

In this work we present the discovery of 72 new ZZ Ceti stars, based on the data from the TESS mission, from sector 1 to sector 39. In addition, we perform follow-up observations for 10 objects from ground-based facilities, i.e., the Konkoly observatory (1.4-m), SOAR telescope (4.1-m) and the Pico dos Dias observatory (1.6-m), which in most cases, increased the number of detected periods. We perform an asteroseismological study of pour sample, and determine the stellar mass, effective temperature and hydrogen envelope mass, among other structural parameters.

The mean stellar mass of our sample from photometry and seismology are $\langle M_{\rm phot}\rangle = 0.572\pm 0.035\,M_\odot$ and $\langle M_{\rm seis}\rangle = 0.613\pm0.015\,M_\odot$, respectively. Considering the 57 objects with photometric masses above 0.49 $M_\odot$, the values are $\langle M_{\rm phot}\rangle = 0.614\pm 0.037\,M_\odot$, and $\langle M_{\rm seis}\rangle = 0.628\pm0.015\,M_\odot$, respectively. Both values are in agreement with the mean mass of a sample of 351 known ZZ Ceti, $\langle M_*\rangle = 0.644\pm0.034\,M_\odot$.

These new 72 ZZ Cetis increase the sample of known pulsating DA white dwarf stars by ∼20%.

ACKNOWLEDGEMENTS

This study was financed in part by the Coordenação de Aperfeiçoamento de Pessoal de Nível Superior - Brasil (CAPES) - Finance Code 001, Conselho Nacional de Desenvolvimento Científico e Tecnológico - Brasil (CNPq), and Fundação de Amparo à Pesquisa do Rio Grande do Sul (FAPERGS) - Brasil. KJB is supported by the National Science Foundation under Award AST-1903828. IP acknowledges support from the UK's Science and Technology Facilities Council (STFC), grant ST/T000406/1. Financial support from the National Science Centre under project No. UMO-2017/26/E/ST9/00703 is acknowledged. ZsB acknowledges the financial support of the Lendület Program of the Hungarian Academy of Sciences, projects No. LP2018-7/2021 and LP2012-31, the KKP-137523 'SeismoLab' Élvonal grant of the Hungarian Research, Development and Innovation Office (NKFIH), and the János Bolyai Research Scholarship of the Hungarian Academy of Sciences.

Based on observations at the Southern Astrophysical Research (SOAR) telescope, which is a joint project of MCTIC–Brazil, NOAO–US, the University of North Carolina at Chapel Hill (UNC), and Michigan State University (MSU), and processed using the IRAF package, developed by the Association of Universities for Research in Astronomy, Inc., under a cooperative agreement with the US National Science Foundation.This paper includes data collected with the TESS mission, obtained from the MAST data archive at the Space Telescope Science Institute (STScI). Funding for the TESS mission is provided by the NASA Explorer Program. This work has made use of data from the European Space Agency (ESA) mission Gaia (`https://www.cosmos.esa.int/gaia`), processed by the Gaia Data Processing and Analysis Consortium (DPAC, `https://www.cosmos.esa.int/web/gaia/dpac/consortium`). Funding for the DPAC has been provided by national institutions, in particular the institutions participating in the Gaia Multilateral Agreement. This research has made use of NASA's Astrophysics Data System Bibliographic Services, and the SIMBAD database, operated at CDS, Strasbourg, France,

DATA AVAILABILITY

Data from TESS is available at the MAST archive `https://mast.stsci.edu/search/hst/ui/$#$/`. Ground based data will be shared on reasonable request to the corresponding author.

REFERENCES

Althaus L. G., Córsico A. H., Bischoff-Kim A., Romero A. D., Renedo I., García-Berro E., Miller Bertolami M. M., 2010, ApJ, 717, 897

Bell K. J., Hermes J. J., Vanderbosch Z., Montgomery M. H., Winget D. E., Dennihy E., Fuchs J. T., Tremblay P. E., 2017, ApJ, 851, 24

Bell K. J., et al., 2019, A&A, 632, A42

Bergeron P., Saumon D., Wesemael F., 1995, ApJ, 443, 764

Bergeron P., Ruiz M. T., Leggett S. K., 1997, ApJS, 108, 339

Bergeron P., Dufour P., Fontaine G., Coutu S., Blouin S., Genest-Beaulieu C., Bédard A., Rolland B., 2019, ApJ, 876, 67

Bognar Z., Sodor A., 2016, Information Bulletin on Variable Stars, 6184, 1

Bognár Z., et al., 2020, A&A, 638, A82

Brickhill A. J., 1991, MNRAS, 251, 673

Castanheira B. G., Kepler S. O., 2008, MNRAS, 385, 430

Chambers K. C., et al., 2016, arXiv e-prints, p. arXiv:1612.05560

Clemens J. C., 1993, Baltic Astronomy, 2, 407

Clemens J. C., Crain J. A., Anderson R., 2004, in Moorwood A. F. M., Iye M., eds, Society of Photo-Optical Instrumentation Engineers (SPIE) Conference Series Vol. 5492, Ground-based Instrumentation for Astronomy. pp 331–340, doi:10.1117/12.550069

Córsico A. H., Althaus L. G., 2006, A&A, 454, 863

Córsico A. H., Romero A. D., Althaus L. G., Hermes J. J., 2012, A&A, 547, A96

Córsico A. H., Althaus L. G., Miller Bertolami M. M., Kepler S. O., 2019, A&ARv, 27, 7

Cowling T. G., Newing R. A., 1949, ApJ, 109, 149

Dolez N., Vauclair G., 1981, A&A, 102, 375

Eastman J., Siverd R., Gaudi B. S., 2010, PASP, 122, 935

Eisenstein D. J., et al., 2006, ApJS, 167, 40

Fontaine G., Brassard P., Bergeron P., 2001, PASP, 113, 409

Fusillo N. P. G., et al., 2021, MNRAS,

Gaia Collaboration et al., 2018, A&A, 616, A10

Gentile Fusillo N. P., et al., 2019, MNRAS, 482, 4570

Gentile Fusillo N. P., et al., 2021, arXiv e-prints, p. arXiv:2106.07669

Giammichele N., Bergeron P., Dufour P., 2012, ApJS, 199, 29

Gianninas A., Bergeron P., Ruiz M. T., 2011, ApJ, 743, 138

Goldreich P., Wu Y., 1999, ApJ, 511, 904

Guidry J. A., et al., 2021, ApJ, 912, 125

Hermes J. J., et al., 2017, ApJS, 232, 23

Istrate A. G., Tauris T. M., Langer N., 2014, A&A, 571, A45

Istrate A. G., Marchant P., Tauris T. M., Langer N., Stancliffe R. J., Grassitelli L., 2016, A&A, 595, A35

Jenkins J. M., et al., 2016, in Chiozzi G., Guzman J. C., eds, Society of Photo-Optical Instrumentation Engineers (SPIE) Conference Series Vol. 9913, Software and Cyberinfrastructure for Astronomy IV. p. 99133E, doi:10.1117/12.2233418

Kepler S. O., 1993, Baltic Astronomy, 2, 515

Kepler S. O., Romero A. D., 2017, in European Physical Journal Web of Conferences. p. 01011 (`arXiv:1706.07020`), doi:10.1051/epjconf/201715201011

Kepler S. O., et al., 2019, MNRAS, 486, 2169

Kilic M., Stanek K. Z., Pinsonneault M. H., 2007, ApJ, 671, 761

Kilic M., Bergeron P., Kosakowski A., Brown W. R., Agüeros M. A., Blouin S., 2020, ApJ, 898, 84

Kleinman S. J., et al., 2013, ApJS, 204, 5

Koester D., 2009, A&A, 498, 517

Koester D., 2010, Mem. Soc. Astron. Italiana, 81, 921

Koester D., Voss B., Napiwotzki R., Christlieb N., Homeier D., Lisker T., Reimers D., Heber U., 2009, A&A, 505, 441

Kowalski P. M., Saumon D., 2006, ApJ, 651, L137

Ledoux P., 1951, ApJ, 114, 373

Lenz P., Breger M., 2004, in Zverko J., Ziznovsky J., Adelman S. J., Weiss W. W., eds, Vol. 224, The A-Star Puzzle. pp 786–790, doi:10.1017/S1743921305009750

Liebert J., Bergeron P., Holberg J. B., 2005, ApJS, 156, 47

Limoges M. M., Lépine S., Bergeron P., 2013, AJ, 145, 136

Montgomery M. H., Hermes J. J., Winget D. E., Dunlap B. H., Bell K. J., 2020, ApJ, 890, 11

Mukadam A. S., Montgomery M. H., Winget D. E., Kepler S. O., Clemens J. C., 2006, ApJ, 640, 956

Murphy S. J., 2015, MNRAS, 453, 2569

Pelisoli I., Vos J., 2019, MNRAS, 488, 2892

Pych W., 2004, PASP, 116, 148

Raddi R., et al., 2017, MNRAS, 472, 4173

Renedo I., Althaus L. G., Miller Bertolami M. M., Romero A. D., Córsico A. H., Rohrmann R. D., García-Berro E., 2010, ApJ, 717, 183

Ricker G. R., et al., 2014, in Oschmann Jacobus M. J., Clampin M., Fazio G. G., MacEwen H. A., eds, Society of Photo-Optical Instrumentation Engineers (SPIE) Conference Series Vol. 9143, Space Telescopes and Instrumentation 2014: Optical, Infrared, and Millimeter Wave. p. 914320 (`arXiv:1406.0151`), doi:10.1117/12.2063489

Romero A. D., Campos F., Kepler S. O., 2015, MNRAS, 450, 3708

Romero A. D., Kepler S. O., Joyce S. R. G., Lauffer G. R., Córsico A. H., 2019a, MNRAS, 484, 2711

Romero A. D., et al., 2019b, MNRAS, 490, 1803

Science Software Branch at STScI 2012, PyRAF: Python alternative for IRAF (ascl:1207.011)

Su J., Fu J., Lin G., Chen F., Khokhuntod P., Li C., 2017, ApJ, 847, 34

Subasavage J. P., Henry T. J., Bergeron P., Dufour P., Hambly N. C., 2008, AJ, 136, 899

Tremblay P. E., Bergeron P., 2009, ApJ, 696, 1755

Tremblay P. E., Bergeron P., Kalirai J. S., Gianninas A., 2010, ApJ, 712, 1345

Tremblay P. E., Bergeron P., Gianninas A., 2011, ApJ, 730, 128

Tremblay P. E., Ludwig H. G., Steffen M., Freytag B., 2013, A&A, 559, A104

Vincent O., Bergeron P., Lafrenière D., 2020, AJ, 160, 252

Wang K., Zhang X., Dai M., 2020, ApJ, 888, 49

Winget D. E., van Horn H. M., Tassoul M., Fontaine G., Hansen C. J., Carroll B. W., 1982, ApJ, 252, L65

This paper has been typeset from a TEX/LATEX file prepared by the author.